Modelling and Optimization of Methane Dehydroaromatization Coupled with Chemical Looping and Temperature Swing Adsorption

Arun Senthil Sundaramoorthy, Sunkyu Kim, Babatunde A. Ogunnaike, Raul F. Lobo,* and Dionisios G. Vlachos*

Department of Chemical & Biomolecular Engineering, University of Delaware, Newark, DE

E-mail: lobo@udel.edu; vlachos@udel.edu

Abstract

Natural gas at remote locations would greatly benefit from on-site processing using modular technologies, such as dehydroaromatization (DHA). This work models an intensified dehydroaromatization process to increase product yield and methane conversion by coupling the reactor with a chemical looping unit that effectively separates hydrogen through a redox cycle and a temperature swing adsorption process to remove the aromatics and water and recycle the unconverted methane. We postulate dynamic models and steady-state surrogate models to analyze and optimize the production of the aromatic product. The optimum methane conversion of 48% and the aromatic yield of 42% occurs at a recycle ratio of 0.47 and a reactor temperature of 725 °C.

1 Introduction

The efficient design and operation of energy systems are pivotal in the reduction of global CO_2 emissions and in driving green, and sustainable manufacturing technologies[1–3]. Methane, a low carbon footprint fuel, can be processed through steam/dry reforming, partial oxidation, nonoxidative coupling, and oxidative coupling[4–6]. The high temperature, pressure, energy requirements, and capital costs of syngas motivates the exploration of direct processes. Moreover, over 30% of natural gas wells are placed in remote areas, making transportation to centralized locations expensive[7–9]. In response, on-site modular dehydroaromatization (DHA) has been proposed as a potential alternative[7,10,11].

The DHA reaction converts methane into aromatics using a Mo/HZSM-5 catalyst at 700 °C[11,12]. The equilibrium-limited nature of the DHA reaction restricts methane conversion to less than 10% at 700 °C[13,14]. To address this limitation, DHA can be coupled with chemical looping (CLC) and temperature swing adsorption (TSA), forming a reactive-separation system based on process intensification principles[15–18]. The CLC consists of metal oxide oxygen carriers that facilitate selective oxidation and reduction reactions, forming a redox loop[19]. In a two-step reaction, the metal oxide donates oxygen to selectively convert hydrogen and is subsequently regenerated by exposure to steam to regenerate the hydrogen. The TSA alternates the temperature of the adsorbent between the adsorption and desorption steps and removes the aromatics. The remaining stream consisting mainly of unconverted methane is recycled to the DHA reactor. [20–23]. Experimental studies on the integrated DHA-CLC-TSA system have demonstrated an aromatic yield of 42% over a four-hour operation, achieving nearly five times higher yields than the thermodynamic limit of DHA at 700 °C[16]. This indicates that the oxidation of hydrogen and the adsorption of aromatics, and water are pivotal for enhanced performance[17,18].

Previous studies have examined the economic impact of modular processes[10], kinetics, and transport properties of DHA[13,14,24], CLC[25–27], and TSA[21,28–30]. For DHA, Mevawala et al.[13] and Razdan et al.[24] developed a multi-scale fixed bed reactor model and analyzed the impact of diffusive length scales of methane with catalyst deactivation. Han et al.[25] presented an extensive process model for a fixed-bed chemical looping reactor, evaluating the impact of transport properties on the rates of different metal-oxide carriers. Zhou et al.[31] discussed a model-driven analysis of experimental chemical-looping reactors with nickel oxide as an oxygen carrier for scale-up studies. Thermodynamic insights on iron-oxide redox reactions were provided by Heidebrecht et al.[26], with subsequent modeling and experimental quantification reported by Hertel et al.[27]. TSA has been studied for CO_2 capture[2,32] and natural gas purification[20,33]. Joss et al.[21] developed a simplified equilibrium model for TSA, focusing on capturing heavy components and determining the operating points and screening materials for CO_2 capture. Similarly, Panikhar et al.[34] provided a performance map for TSA, determining energy requirements, the range of product recovery, and process capacity. Yet, the operating limits of these individual processes and their impact on the synergistic effects observed on the conversion and productivity of the integrated DHA process have not been investigated.

In process engineering, the integrated DHA-CLC-TSA process shares similarities with a reaction separation involving recycling, as discussed in various reports[35–43]. Denn et al.[41] and Morud et al.[36] have examined the impact of plant dynamics for activated sludge process, autothermal process, and other arbitrary chemical processes, noting that recycling of mass or energy can behave like a positive feedback controller (negative gain), potentially leading to instability in plant behavior. Larsson et al.[35] and Kumar et al.[38] have systematically investigated operating variables and dynamics of time-scale separation for the effective operation of processes involving reactive separation with recycling. Griffin et al.[37] and Baldea and co-workers[39,40,44] discussed the impact of selecting process units, considering reaction chemistry, trade-offs between conversion and selectivity, limitations associated with integrating processes that incorporate recycling, along with equation oriented pseudo-transient simulation method for the salicylic acid nitration, ammonia synthesis network, and arbitrary sequence of first-order reactions.

A systems-level understanding of the operation of the entire system is important, given its complexity[16]. Despite the past progress in reactive separation processes and a stand-alone understanding of DHA, CLC, and TSA processes, the operating limits of complex reactive separation systems are still unavailable. When experimental data is sparse and expensive to obtain, model-based methods can provide valuable insights. The first objective of this work is to develop a model for an integrated DHA-CLC-TSA process (Figure 1)[15,16], determine the achievable aromatics yield and methane conversion, and understand the operation of each process. Each process is simulated using a one-dimensional spatiotemporal model. To balance computational efficiency and accuracy, surrogate models for all processes are developed[45–47], integrated, and simulated using a simultaneous modular method[48,49]. The second objective is to optimize the product yield and conversion by manipulating the recycle ratio[35,37] using Lagrange multipliers[50,51]. The optimization problem is solved with operational and economic objectives resulting in an optimum recycle ratio ($\mathrm{R}_{\mathrm{recycle}} = 0.47$) and a DHA operating temperature of 725 °C to achieve an economic trade-off between product yield and conversion of methane.

2 Materials and Methods

2.1 Process Overview

The experimental integrated modular process, investigated by Brady et al., 2021[15,16], consists of three fixed beds connected in series: DHA, CLC, and TSA, as illustrated in Figure 1. Within the DHA unit, methane undergoes selective conversion into hydrogen and aromatics over a 2 wt % Mo/H-ZSM5 (400 mg) catalyst at 700 °C. The catalytic reaction involves three stoichiometric steps (Eq. 1). Methane is converted to ethylene as the primary product of C-C coupling. Subsequently, ethylene trimerizes into benzene and hydrogen. Finally, ethylene and benzene combine to form naphthalene and additional hydrogen.

$$\begin{aligned} \mathrm{R_1}:\ 2\ \mathrm{CH_4} &\rightleftharpoons \mathrm{C_2H_4} + 2\ \mathrm{H_2} \\ \mathrm{R_2}:\ 3\ \mathrm{C_2H_4} &\rightleftharpoons \mathrm{C_6H_6} + 3\ \mathrm{H_2} \\ \mathrm{R_3}:\ \mathrm{C_6H_6} + 2\ \mathrm{C_2H_4} &\rightleftharpoons \mathrm{C_{10}H_8} + 3\ \mathrm{H_2} \end{aligned} \tag{1}$$

The desired overall reaction converts methane into benzene as illustrated in Eq. 2.

$$6\ \mathrm{CH_4} \rightarrow \mathrm{C_6H_6} + 9\ \mathrm{H_2} \tag{2}$$

Thermodynamic equilibrium severely limits the single-pass conversion of methane to be 7% to 12% with aromatics yield of 10% at 700 °C under atmospheric pressure[11,52]. Hence, CLC is placed downstream of the DHA process to remove hydrogen and recirculate unconverted methane. A metal oxide (7 g of $\mathrm{Fe_3O_4}$) converts hydrogen into water, FeO, and Fe at 650 °C.

$$\mathrm{Fe_3O_4} + \mathrm{H_2} \rightleftharpoons 3\mathrm{FeO} + \mathrm{H_2O} \tag{3}$$

In TSA, benzene and naphthalene from the DHA and water from the CLC are removed with zeolite 13X (10 g) at 80 °C.

$$\begin{aligned} \mathrm{C_6H_6} + \mathrm{Ads} &\rightleftharpoons \mathrm{Ads}\cdot\mathrm{C_6H_6} \\ \mathrm{C_{10}H_8} + \mathrm{Ads} &\rightleftharpoons \mathrm{Ads}\cdot\mathrm{C_{10}H_8} \\ \mathrm{H_2O} + \mathrm{Ads} &\rightleftharpoons \mathrm{Ads}\cdot\mathrm{H_2O} \end{aligned} \tag{4}$$

The unconverted methane and leftover products are recirculated at 20 SCCM into the DHA reactor. Fresh methane is introduced from a bleed tank (BT) to replenish the methane. In terms of gas hourly space velocity (GHSV in mL/g.h), 20 SCCM equivalent is 3000 GHSV in DHA, 180

GHSV in CLC, and 125 GHSV for the TSA. These are the nominal laboratory values.

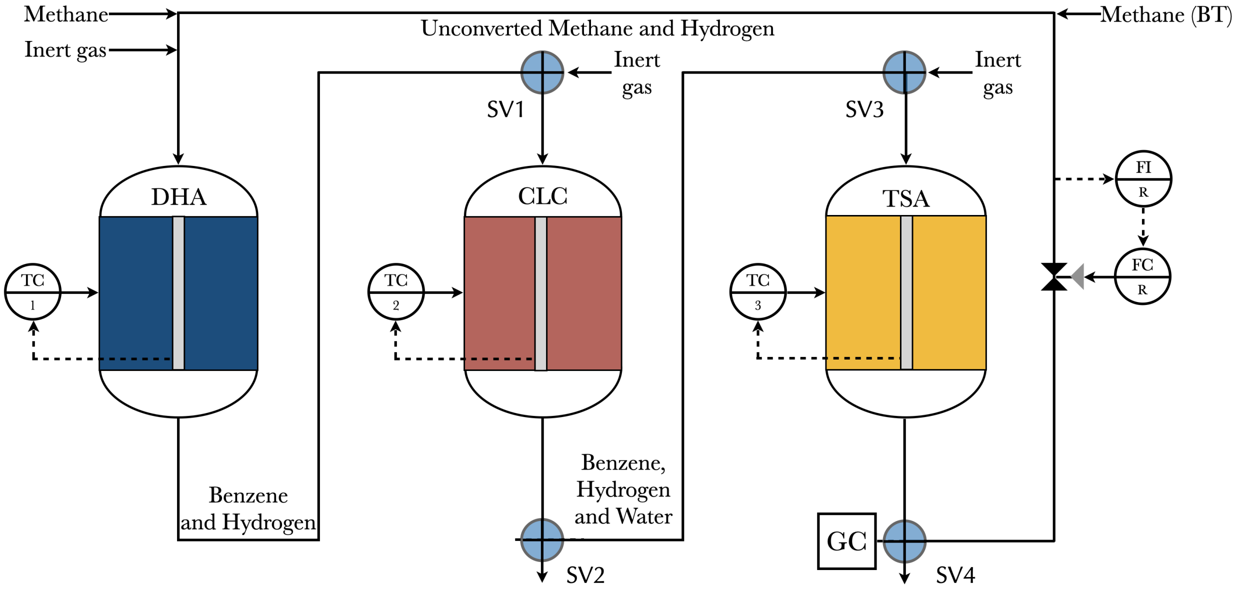

Figure 1: *Schematic of integrated methane dehydroaromatization process flow-sheet. The sequence of process units and individual stream's component information and control structure is shown with fresh methane feed from the bleed tank (BT).*

Binary process configurations, such as DHA-CLC and DHA-TSA, have been investigated experimentally[16]. In the DHA-CLC configuration, an approximately 16% methane conversion was achieved at the end of a four-hour run. Traces of aromatics were detected in DHA, yet these were converted into CO and CO_2 due to a reforming reaction induced by steam generated in the CLC bed as a result of Fe_3O_4 reduction. In the DHA-TSA configuration, the methane conversion reached 24.6%, with aromatics captured in the molecular sieve at a yield of 10.8%. The integration of all three processes led to a significant improvement in overall methane conversion of 50% and aromatics yield of 42% at the end of a four-hour operation.

2.2 Process Models

We build and analyze the spatiotemporal behavior of each packed-bed unit and their collective behavior. The approach involves four steps (Figure 2). In the randomized sampling of process variables step, we utilize Latin hypercube (LH) sampling, a method that intelligently selects conditions such as inlet concentration, flow rate, and temperature. The boundaries for this sampling are determined based on the literature[16]. We simulate the system at the suggested conditions.

In the unit model development step, we formulate mathematical models for the spatiotemporal behavior of the packed-bed units and solve them at LH-sampled initial conditions to obtain the end concentrations. We utilize the published reaction rate and adsorption kinetic parameters[27,53,54]. In the surrogate model construction step, we train simpler surrogate models, using exit concentration data from numerical simulations as the output with LH samples as inputs, as approximations of the full models. Lastly, the system's yield is optimized using the surrogate models to determine optimal operational conditions in the yield optimization step. This approach provides a foundation for understanding and optimizing integrated reactive separation process systems.

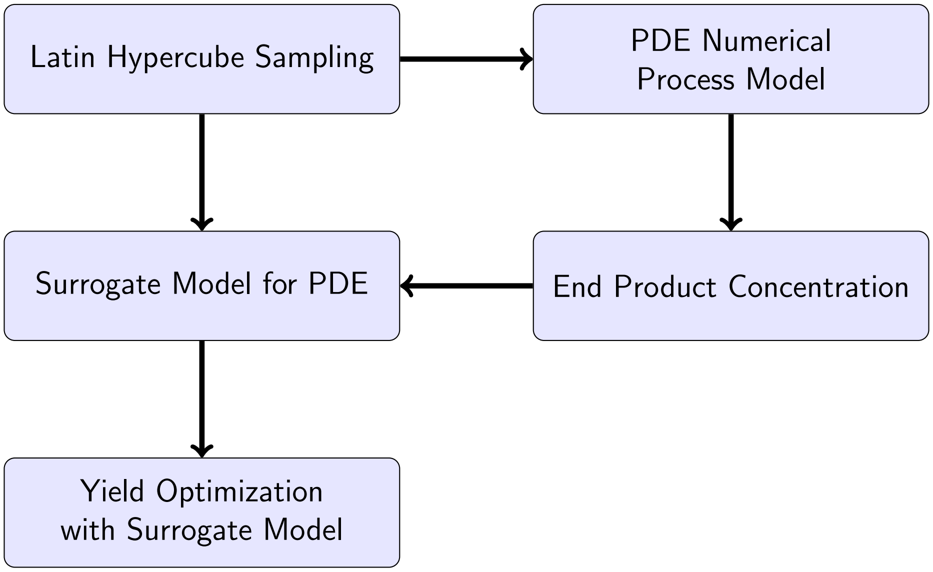

Figure 2: *Model development workflow for the integrated DHA-CLC-TSA process. The main workflow includes sampling operating conditions, such as concentration (C), inlet flow rate (Q), and temperature (T), using Latin hypercube (LH) sampling, numerical and surrogate model development using the LH samples as initial conditions, and as the inputs. Finally, yield is optimized using the surrogate models.*

Each process is described using a dimensionless convection-diffusion-reaction transport model in one dimension

$$\frac{\partial \bar{\mathbf{C}}}{\partial \tau} = -\alpha_{\xi}\frac{\partial(\bar{\mathbf{C}})}{\partial \xi} + \frac{1}{\mathsf{Pe}}\frac{\partial^2 \bar{\mathbf{C}}}{\partial \xi^2} + \mathsf{Da}(\bar{\mathbf{C}}, \Theta) \tag{5}$$

where $\bar{\mathbf{C}}$ is the dimensionless concentration $\bar{\mathbf{C}} = \frac{\mathbf{C}}{C_0}$, $\mathsf{Pe} = \frac{v_0 L}{D_e}$ is the Péclet number, $\mathsf{Da} = \frac{\mathsf{R}(C)}{C_0}\frac{L}{v_0}$ is the Damköhler number, $\alpha_{\xi} = \frac{v_{\xi}}{v_0}$ is the dimensionless velocity, $\xi = \frac{z}{L}$ is the dimensionless length of the fixed-bed, and $\tau = \frac{v_0 t}{L}$ is the dimensionless time. C is spatiotemporal concentration and C_0 is the inlet concentration of each component. The units of concentrations are $\frac{kmol}{kg_{cat}}$ for catalytic reactions and $\frac{kmol}{kg_{solid}}$ for gas-solid non-catalytic reactions and separations. $R(C)$ is net-rate of gas-phase species formation in $\frac{kmol}{kg_{cat}\cdot s}$, t is time in seconds (s), L is the length of the fixed bed (m), v_0 and v are superficial and interstitial velocities of the gas-phase components ($\frac{m}{s}$), and D_e is either the diffusivity or dispersion coefficient ($\frac{m^2}{s}$).

The parabolic partial differential equations (PDE) model in Eq. 5 is solved subject to initial and boundary conditions. The initial condition is set as $\bar{\mathbf{C}}(\xi, 0) = 1$, while Dirichlet and no flux Neumann boundary conditions are applied at the inlet and the outlet, represented as $\bar{\mathbf{C}}(\xi = 0, \tau) = 1$ and $\frac{\partial \bar{\mathbf{C}}}{\partial \xi}|_{(\xi=1,\tau)} = 0$, respectively. Alternatively, mixed boundary conditions (Danckwerts type) can be used at the inlet, expressed as $\bar{\mathbf{C}}(\xi = 0, \tau) = \bar{\mathbf{C}}_{in} + \frac{1}{\mathsf{Pe}}\frac{d\bar{\mathbf{C}}}{d\xi}$. The radial gradients are neglected due to the small bed diameter-to-bed length ratio and the high particle-to-bed diameter ratio. In standard laboratory scale reactor design practices, a ratio $\frac{L}{d} > 5$ ensures plug flow behavior. The Damköhler number (Da) in Eq. 5, describing the relationship between reaction and transport time scales, varies for each unit. Further details are expounded upon in subsequent sections.

The variables and parameters related to DHA, CLC, and TSA are represented with subscripts $(\cdot)_1$, $(\cdot)_2$, and $(\cdot)_3$, respectively. In DHA, H-ZSM5 catalyst deactivation is taken into account. Each product with two or more carbons leads to deactivation[55–57]. The zeolite catalyst deactivation is modeled as second-order kinetics and the activity information is incorporated with the DHA reaction rates as suggested in the literature[55,56]. The deactivation rate model information is in the S.I. For CLC and TSA, diffusion/dispersion terms are excluded due to the high Peclet number, transforming the parabolic PDE into a hyperbolic PDE. Additionally, model equations for the solid phase (iron-oxide in CLC and zeolite-13x in TSA) are also included. Subsequently, nonlinear wave theory applied to the hyperbolic PDE indicates fast mass transfer between two phases (gas-solid), establishing local equilibrium between phases[58]. The transport model for gas-phase species in CLC is presented in the SI (Eq. 18) and the model for the solid-phase (iron oxide) reaction is

$$\frac{\partial x_{\mathsf{Fe_3O_4}}}{\partial \tau_2} = \left(\frac{\epsilon_g}{1-\epsilon_g}\right)(-r_{clc})\left(\frac{L_2}{v_{0_2}}\right) = \mathsf{Da}_s \tag{6}$$

where (r_{clc}) (Eq. 14 in SI) represents the redox reaction kinetics for hydrogen consumption (moles of Fe_3O_4 per m^3 of solid particle), ϵ_g is the porosity of iron oxide bed, L_2 is the bed length (cm) and v_{0_2} is superficial velocity (cm/s). In this context, Da_s denotes the Damköhler number for the gas-solid reaction.

In TSA, the gas-phase transport model is described in SI (Eq. 20). Going beyond the standard Langmuir adsorption isotherm, interactions among adsorbing species are considered[59].

A generic expression for the Langmuir isotherm with interactions is

$$q_i^* = q_{s_i} \frac{b_i p_i + R_i (b_i p_i)^2 + R_{ij}(b_i p_i b_j p_j)}{\left(1 + \sum_{k=1}^{n=3}(b_k p_k + 0.5 R_k (b_k p_k)^2)\right) + R_{ij}(b_i p_i b_j p_j)} \tag{7}$$

Here $p_i = C_i RT$ is the partial pressure (atm), $q_{s_i} = (q_0)_i \times e^{-\frac{\Delta E_i}{RT}}$ is the site density $(\frac{kmol}{kg_{zeo}})$, $b_i = (b_0)_i \times e^{-\frac{\Delta H_i}{RT}}$ is the Langmuir constant (atm^{-1}), ΔE_i and ΔH_i are molecular energies $(\frac{kJ}{kmol})$, R_i is the interaction parameter between a molecule (i) and the zeolite, R_{ij} is the binary interaction between molecules i and j. The interaction parameters are computed using partial pressures of the adsorbing species. The expression to compute these parameters is presented in SI (Eq. 21 and Eq. 22). Due to the Onsager reciprocal relation, a symmetry constraint is imposed on the cross-molecule interaction parameter as $R_{ij} \equiv R_{ji}$. In the absence of interactions, i.e., when R_i and R_{ij} are 0, Eq. 7 reduces to the conventional Langmuir isotherm model. When $R_i > 1$, attractive forces dominate, and vice versa for $R_i < 1$. Detailed models for CLC and TSA are provided in the SI sections B and C. The reaction kinetics and associated model parameters for all processes are available in the SI sections D to F.

The transient PDEs are discretized using the finite difference method, Method of Lines, as detailed in references[60–62]. We employ upwind (for convective terms) and central finite difference (for diffusive terms) for spatial discretization. Inlet and outlet boundary conditions are discretized using a backward (mixed type) scheme and a forward difference (Neumann) scheme, respectively. The resulting system takes the form of a set of stiff nonlinear Ordinary Differential Equations (ODEs), organized in an input/output structure. This configuration aligns with constructing a nonlinear state-space model within the systems and control community, as documented in[63,64]. Concurrently, the pressure drop in the reactor is computed with Eq. 5 using Ergun's equation (Eq. 8)

$$\frac{\mathrm{d}P}{\mathrm{d}\xi} = -\frac{150\mu_g(1-\epsilon_b)^2(L\alpha_\xi v_0)}{d_p \epsilon_b^2} - \frac{1.75\rho_g(1-\epsilon_b)L(\alpha_\xi v_0)^2}{d_p \epsilon_b} \tag{8}$$

In Eq. 8, the viscosity of the gas mixture, μ_g, is computed using Wilke's method[65,66]. d_p and ϵ_b denote particle diameter and bed porosity, respectively.

2.3 Surrogate Process Models and Process Integration

The spatiotemporal process dynamics of DHA, CLC, and TSA across three distinct process time scales need to be integrated and solved inexpensively. We opt for a simulation data-driven approach to construct surrogate models[45–47]. Mathematically, a surrogate model is described as:

$$\hat{\mathsf{Y}} = \mathsf{F}_{\mathsf{surrogate}}(\mathsf{X}, \Theta) + \epsilon = f(\mathsf{X})^T \Theta + \epsilon \tag{9}$$

Here, $\mathsf{X} \in \mathbf{R}^{n_x}$ represents the input for the model, $\hat{\mathsf{Y}} \in \mathbf{R}^{n_y}$ the output and Θ the model parameters to be estimated. $\hat{\mathsf{Y}}$ signifies the exit concentrations in the DHA, CLC, and TSA processes at a specified operating time. The term ϵ represents model approximation error, modeled statistically as a white noise[45,47]. The input X comprises the dimensionless concentration, flowrate, and temperature ($\left[\bar{\mathsf{C}}\ \bar{\mathsf{Q}}\ \bar{\mathsf{T}}\right]$). The input variables are subjected to simple nonlinear transformation expressed as $f(\mathsf{X}) = \left[\mathsf{X}\ \sqrt{\mathsf{X}}\ \log(\mathsf{X})\ \mathsf{X}^{-1}\right]^{d}$[67,68]. The value of d defines the polynomial order of $f(\mathsf{X})$, selected using the process knowledge. In this work, coefficient of the logarithm of the Damköhler number is selected as the value of d.

Data points for $\hat{\mathsf{Y}}$ are generated using Latin hypercube sampling in X (Figure 2). The surrogate model, Eq. 9, is a nonlinear model with a linear-in-parameter form. Due to the linearity, the parameters can be estimated using least square optimizers[50,69–71]. An ensemble of machine learning models was explored to predict the output, including random forest and XGBoost[72], conventional linear regression[71], non-parametric regression, like Kernel and Gaussian process regression with squared exponential and Matern kernel as basis functions[73], and constrained regression methods like l_0 regression[69,74] and its convex variant LASSO[71,75].

All methods, except conventional linear regression, have tunable hyper-parameters. The hyper-parameters of ensemble and non-parametric surrogate models are optimized using Bayesian optimization, and those of constrained linear regression models, hyper-parameters are optimized using the Akaike information criterion (AIC). The models undergo training using n-fold cross-validation, with 70% of samples for training and the remaining for testing. The surrogate model's performance is evaluated using the root mean square error (RMSE) and mean absolute error (MAE). These surrogate models are then employed for process integration and optimization.

The surrogate models are coupled, as the output of one model becomes the input of another with a simple mixing equation for the recycle stream. The mathematical representation of the model integration is presented in Section F of the SI. In SI, Eq. 25, $\mathsf{R}_{recycle} \in [0, 1]$ is the recycle ratio used to determine the recycle flowrate $\mathsf{Q}_{recycle} = \mathsf{R}_{recycle} * \mathsf{Q}_{flow}$. The tearing method is employed to solve the surrogate model equations[48] (SI Eq. 25), where the value of the recycle stream is determined using a Picard-like iteration in predictor-corrector form. The iterative sequence is described in Eq. 26 in the SI. The model outcomes are quantitatively assessed in terms of yield and selectivity vs methane conversion per pass and the recycle ratio. The integrated surrogate models are effective in representing a high-dimensional system.

2.4 Process Optimization

The optimization objectives include maximizing the product yield and the methane conversion per pass and are posed as a multi-objective problem[50,70,76]. Further, operational constraints are incorporated based on experimental limitations[16]. The details of the constrained optimization problem are presented in Section H of the SI (Eq 29 and Eq 30). The multi-objective cost and constraints are presented as

$$\begin{aligned}
J(\mathsf{u}=\mathsf{R},p) &: \omega\Phi_1 + (1-\omega)\Phi_2 \\
\mathsf{g}_1(\mathsf{u},p) &: \sum_i \mathsf{x}_i - 1 \leq 0, \forall\, i = 1 : n_x \\
\mathsf{g}_2(\mathsf{u},p) &: \mathsf{R}_{recycle} - \mathsf{R}_{max} \leq 0 \\
\mathsf{g}_3(\mathsf{u},p) &: \mathsf{R}_{min} - \mathsf{R}_{recycle} \leq 0
\end{aligned} \tag{10}$$

where $J(\cdot)$ is a nonlinear objective function, Φ_1 and Φ_2 are the product yield and methane conversion. The prices of benzene, naphthalene, and methane, $\mathsf{p}_{C_6H_6}$, $\mathsf{p}_{C_{10}H_8}$ and p_{CH_4}, are incorporated as coefficients in Φ_1 and Φ_2. $\omega \in [0,1]$ is the weight between objectives. $\mathsf{R}_{recycle}$ is the decision variable [35,37]. $\mathsf{R}_{max} = 0.98$ and $\mathsf{R}_{min} = 0.25$ are the upper and lower limits. p is a vector accompanying the flow rate and the temperature. For every optimal guess, R^k, computed using SI Eq. 30, the system of surrogate models is solved until convergence. The optimization problem provides the optimal temperature, yield, and ω. The structure of the optimization problem remains the same for operational and economic optimization. The major difference is that the price of components is ignored in conventional optimization. The details of the objectives are provided in the SI (Eq. 31).

3 Results and Discussion

3.1 Parametric Analysis of Dehydroaromatization (DHA)

The results of the DHA parametric analysis (Figure 3A and B) show that the DHA process reaches a quasi-steady state within the first sixty minutes of the total operating period of four hours. Ethylene reaches a quasi-steady state first, followed by benzene and naphthalene. Spatially, ethylene shows a non-monotonic profile with the maximum value reached near the middle of the fixed bed; benzene and naphthalene attain a maximum value downstream. This is reflected in the product yield and selectivity (Figure 3C). At the reactor exit, benzene achieves a maximum carbon selectivity exceeding 60% with a yield of 7% followed by naphthalene (selectivity 5.2% and yield 0.5%) and ethylene (selectivity 1.2% and yield under 0.2%) at 700 °C and 1 atm pressure. Toward the end of the reactor, naphthalene yield surpasses that of ethylene. Simulated product yields align with existing literature, with total product yields around 6 to 10%. Figure 3C also indicates that the steady-state methane conversion of 9% is limited by thermodynamics[14–16,77].

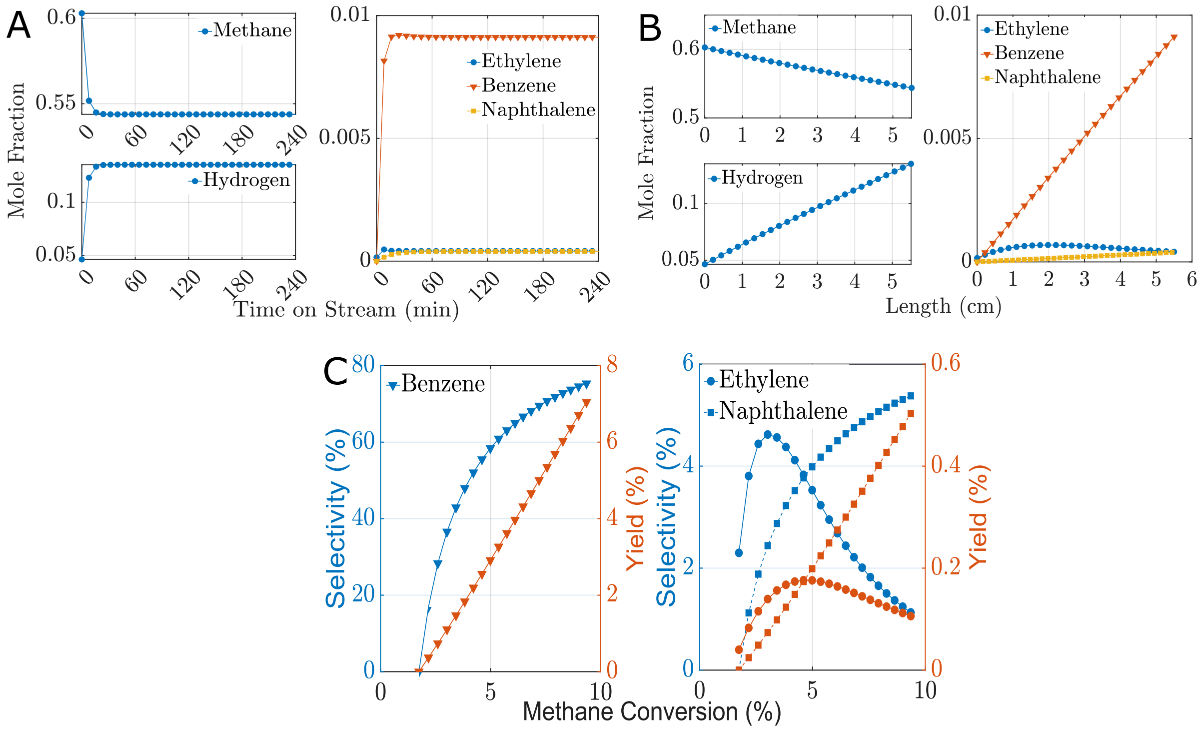

Figure 3: *DHA process analysis. The reactant (methane), products (ethylene, benzene, naphthalene, and hydrogen), and unconverted methane mole fractions at the reactor exit at different time instants, and the corresponding spatial profiles along the fixed bed. A. Exit mole fraction of methane and products vs. time. B. Mole fractions vs. reactor bed length at the end of four hours at steady-state. C. Selectivity (right axis) and yield (left axis) of carbon products vs. methane conversion.*

The statistical relationship between the input-output and product yields is analyzed using correlation analysis (SI Figure 10). Ethylene, benzene, and naphthalene in the feed positively affect benzene yield, while hydrogen in the outlet has a negative impact on the benzene yield. This observation agrees with the literature[11,77], where hydrogen in the outlet limits aromatics yield due to chemical equilibrium.

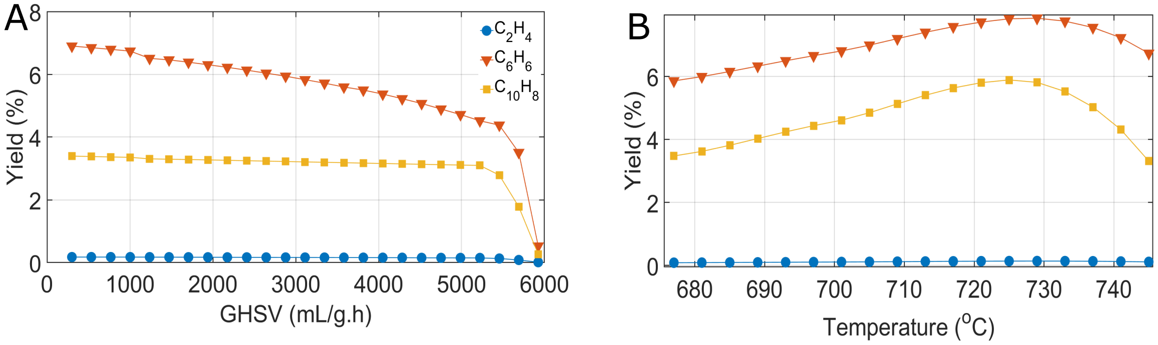

Figure 4: *Effect of flow rate and temperature on DHA. A. Effect of flow rate on product yields evaluated at* $C_{CH_4,in} = 0.7\frac{mol}{m^3}$ *and* $C_{He,in} = 0.3\frac{mol}{m^3}$ *at 700°C. B. Effect of temperature on product yields evaluated at* $C_{CH_4,in} = 0.7\frac{mol}{m^3}$ *and 3000 mL/g.h.*

The product yield decreases monotonically as the flow rate increases due to decreasing residence time (Figure 4A and B). The product yield declines substantially above a space velocity of 5000 mL/g.h due to the reaction zone moving to the reactor exit. An increase in the methane-to-inert ratio in the feed enhances the product yield. Below 680 °C, experiments show no activity[11,52], and above 730 °C, benzene selectivity decreases due to rapid naphthalene formation. This trend is evident in Figure 4B, where the product yield exhibits a maximum at 730 °C. This observation suggests that operating DHA at or below 730 °C and 5000 mL/g.h is suitable.

3.2 Parametric Analysis of Chemical Looping Combustion (CLC)

In the CLC, hydrogen reacts with Fe_3O_4 to form water. Hertel et al. and Heidebrecht et al.[26,27] suggest that once equilibrium is reached between Fe_3O_4 and hydrogen, the reaction zone propagates along the axial direction, generating a moving front. This is presented in Figure 5A, displaying the progress of the equilibrium front of hydrogen and water at different times. Initially, the equilibrium front velocity of hydrogen and water remains constant, however, as water forms, the waterfront velocity decreases, and the equilibrium front is convected down the bed, displaying a lag in water reaching the equilibrium conversion. This phenomenon is due to the interplay between kinetics and transport, where the concentration of hydrogen and water governs the components' interstitial velocity (See species velocity expression in the SI). Figure 5A also illustrates that 20% of the total bed (1 cm of the 5 cm) is utilized in a single-pass operation of 4 h, and indicates that equilibrium is reached after consuming 40% of the initial hydrogen. This aligns with literature findings based on the Bauer-Glaessner thermodynamic diagram for hydrogen-water over iron-oxide and it indicates that the length of an iron-oxide bed could be halved without detriment or the operation can be extended[16,26,27].

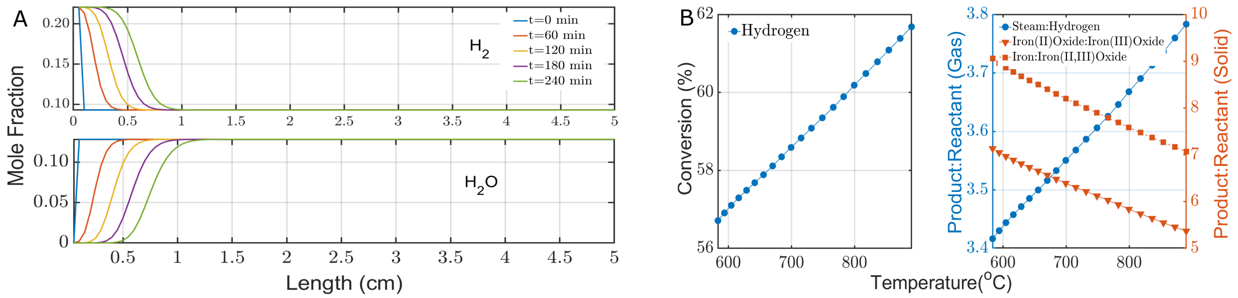

Figure 5: *CLC process analysis. A. Spatial response of hydrogen and water at different times in min. B. Hydrogen conversion, and ratio of product-to-reactant of gases and solids w.r.t temperature.*

Figure 5B presents hydrogen conversion and the product-to-reactant ratio as a function of temperature. Due to the reaction endothermicity, an increase in temperature increases the hydrogen conversion (Figure 5B). The variation in hydrogen conversion with temperature is relatively small (Figure 5B). The water-to-hydrogen ratio increases with temperature. Conversely, the ratio of FeO to Fe_3O_4 and Fe to Fe_3O_4 decreases with temperature. This is also due to the presence of Fe_3O_4 in excess compared to FeO and Fe at high temperatures[26]. Given the opposing trends in the gas phase and solid phase product-to-reactant ratios (Figure 5B), the desired operating temperature should be between 680 and 770 °C.

3.3 Parametric Analysis of Temperature Swing Adsorption (TSA)

A Langmuir isotherm was applied to model the adsorption of an ideal ternary mixture of benzene, naphthalene, and water on zeolite-13X, incorporating a linear driving force (LDF) model. In this model, the breakthrough time and the saturating distance in the axial direction of the equilibrium front are similar for water, naphthalene, and benzene. The experiments indicate complete adsorption of benzene, naphthalene, and water by the zeolite-13X[16]. However, considering the non-ideal nature of the mixture and interactions with the zeolite-13X framework, additional simulations were conducted using a competitive interaction Langmuir isotherm model (Eq. 7). Figure 6A reveals significant variations in the saturating region of the bulk-phase concentration profile of the adsorbing components after 4h. The relatively sharper concentration front of benzene and naphthalene compared to water is due to differences in the heats of adsorption, resulting in competitive adsorption of aromatics upstream, and water downstream. Without interactions, only 18% of the total zeolite bed is saturated. In total, only 12% of the total bed is saturated by benzene and naphthalene, and 24% by water (Figure 6A).

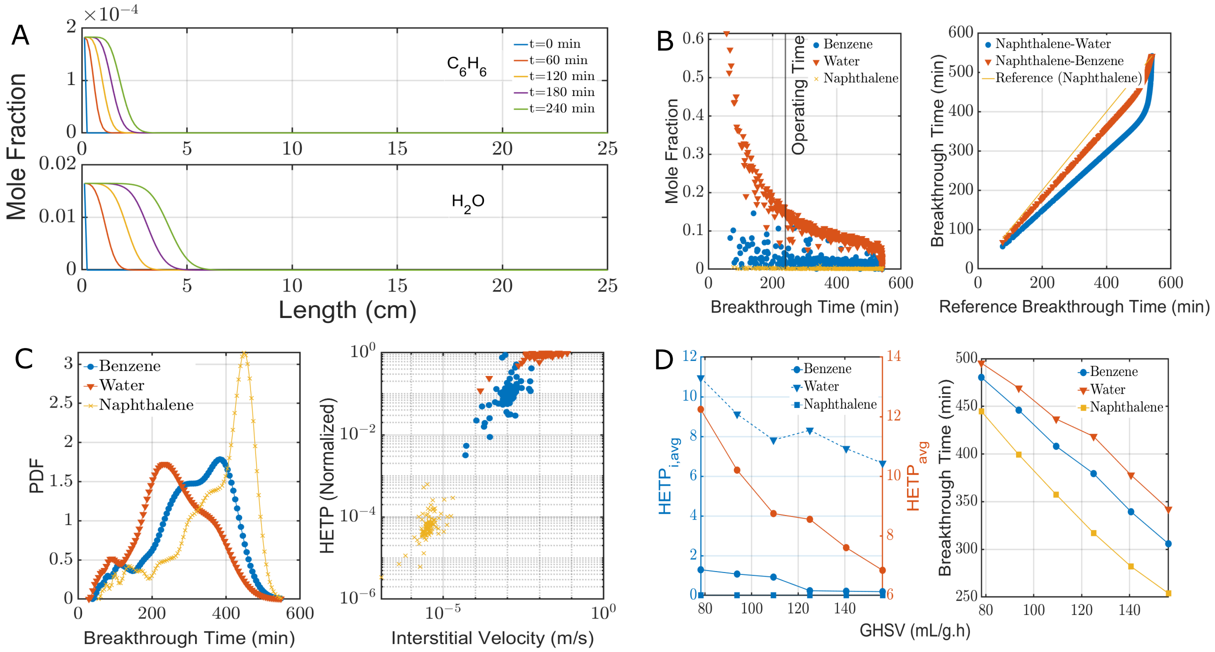

Figure 6: *Analysis of temperature swing adsorption process. A. Spatial response of benzene and water at different times. B. Impact of inlet mole fraction of benzene, naphthalene, and water on breakthrough time. Comparison of breakthrough time w.r.t naphthalene. C. Kernel density of breakthrough time for adsorbing species and log-log HETP w.r.t interstitial velocity. D. Average HETP and breakthrough time w.r.t flowrate.*

A parametric analysis was performed by varying the inlet feed concentration and its flow rate for 9 h to map the design space and operating limits of the bed (Figure 6B, C, and D). The breakthrough time vs. inlet concentrations for a fixed space velocity of 125 mL/g.h is shown in Figure 6B. The operating time of 4h is indicated by a vertical line to determine the concentrations at which breakthrough occurs. The column saturates quickly for the inlet concentrations left of the operating timeline (high concentration regime) and exhibits a shorter breakthrough time. For feed concentrations, the right of the operating timeline (low concentration regime) saturation of the bed takes sufficiently longer. The right plot in Figure 6B shows the deviation of breakthrough time w.r.t the strongly adsorbed species (naphthalene), which indicates water breakthrough first followed by benzene and naphthalene.

Statistical measures and process-oriented metrics, such as kernel density estimators and the height equivalent theoretical plate (HETP), were employed to determine the average breakthrough time of each species and the location of adsorbing species by characterizing the impact of external mass transfer and convective time scales. Figure 6C indicates that naphthalene's average breakthrough time (440 min) is greater than benzene (1.25 times) and water (2.25 times). HETP indicates that naphthalene predominantly adsorbs at the entrance of the bed, benzene in the middle region, and water toward the exit. Water exits first due to its adsorption location and can be used as an indicator of column saturation. Further, adjusting the flow rate w.r.t feed concentration is essential to prevent the column from reaching saturation. HETP and breakthrough time decrease with increasing volumetric flowrate (Figure 6D), indicating insufficient residence time for the species to adsorb. Hence, a space velocity of 125 mL/g.h or lower or a longer bed is recommended.

Further, statistical tools such as KL-divergence[78], and the Wasserstein metric[79], were also used to quantify the effect of flowrate on the breakthrough time distribution of the adsorbing species (Figures 11 and 12 in the SI).

3.4 Integrated Process Model

The surrogate models are computationally cost-effective to integrate and analyze the entire process. The models are trained using the full models for a wide range of inlet concentrations, temperatures, and flow rates. The surrogate model predictions of species mole fractions are within 5% of the full model (error statistics are in Figures 13 and 14 in the SI). The findings from the integrated surrogate models are shown in Figures 7 and 8. The methane mole fraction in the reactor exit starts at 61% and decreases linearly to 53% with an increase in recycle ratio (Figure 7A) i.e., 40% to 60% of methane is converted for a feed with 95% methane, which is seven times more than the stand-alone DHA process (Figure 7B). The aromatics and hydrogen mole fractions decrease with an increase in the recycle ratio (Figure 7A). Yet, the average exit mole fraction in the integrated process increases by 1.5 to 6 times compared to the stand-alone DHA process (Figure 7B). When the percentage of methane in the feed decreases by 20%, methane conversion increases by 1%. However, the aromatics mole fraction decreases proportionately (Figure 15 in the S.I). The hydrogen conversion in CLC ranges from 32% to 45% (Figure 7C). Thermodynamics of iron-oxide phase equilibrium establishes a conversion of 38% hydrogen. Operating at a recycle ratio of 0.5 or below provides the necessary hydrogen conversion.

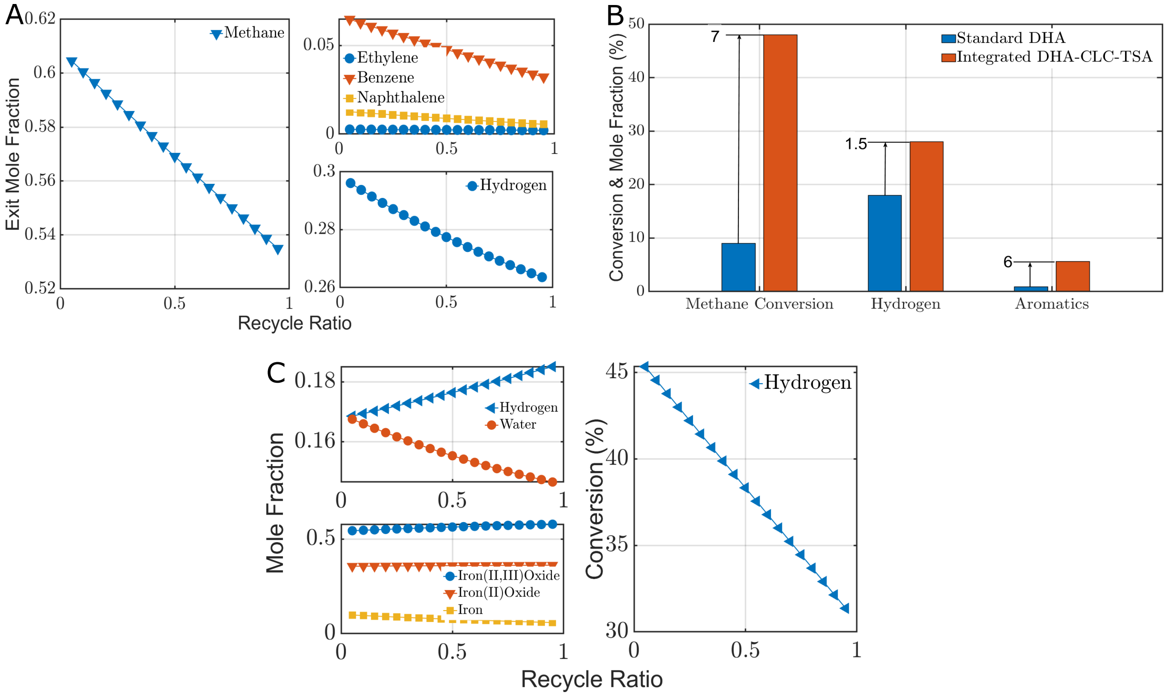

Figure 7: *A. Exit mole fractions vs recycle ratio in the DHA process. B. Conversion and product mole fraction comparison between the standard and integrated DHA. C. Exit mole fractions vs recycle ratio in the CLC process.*

The yield and selectivity per pass monotonically decrease with an increase in methane conversion per pass. Similarly, product yield decreases with an increase in the recycle ratio (Figure 8A and B). These observations are highly correlated; at a lower recycle ratio, the number of recycle passes is significantly lower compared to a higher recycle ratio (Figure 8B). Due to the variations in recycle passes, residence time affects the methane conversion per pass proving that the recycle ratio is pivotal for achieving desired process yields. The operating boundary line in Figure 8C indicates that naphthalene formation increases until a recycle ratio of 0.55, and above that, the rate of reaction forming naphthalene decreases. This is reflected in the benzene-to-naphthalene ratio, which increases rapidly for R > 0.55. This result is consistent with the analysis in Figure 8A and B and the selectivity-conversion profiles in the literature[37,80,81].

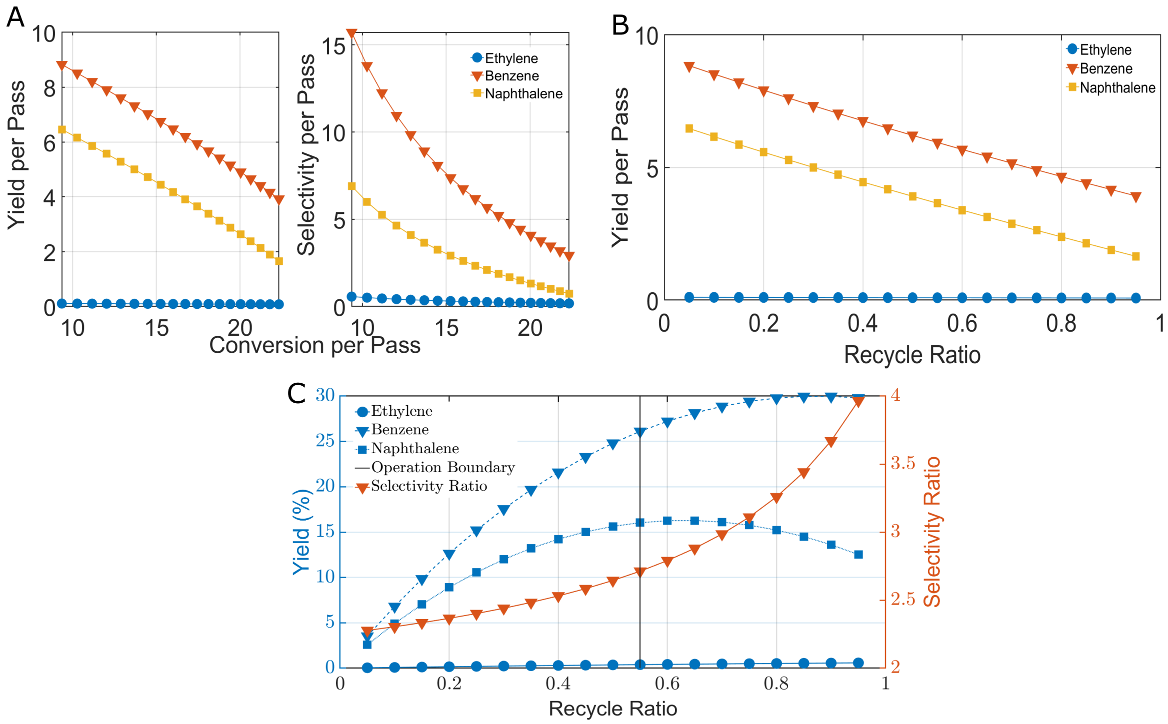

Figure 8: *Analysis of surrogate models. A. Yield and selectivity per pass w.r.t methane conversion per pass. B. Yield per pass w.r.t the recycle ratio. C. Product yield and selectivity ratio w.r.t recycle ratio.*

3.5 Optimization of Product Yields

The product yields are optimized for operational and economic objectives with constraints on the optimization variable. The objective function outlined in Eq. 10 is evaluated based on the surrogate model (Eq. 26). The Pareto weights (ω) were adjusted to account for different recycle ratios (R). When ω is set to zero, the methane conversion at every pass is optimized, while at $\omega = 1$, the overall aromatics yield at the end of recycle is optimized. Furthermore, at a high recycle ratio, the objective function optimizes the methane conversion, and a low recycle ratio prioritizes optimizing yield over the methane conversion. Throughout the analysis, the DHA temperature was fixed at 700, 725, and 745 °C. Due to the non-monotonic nature of the aromatics yield, operating at an intermediate temperature of 725 °C is recommended.

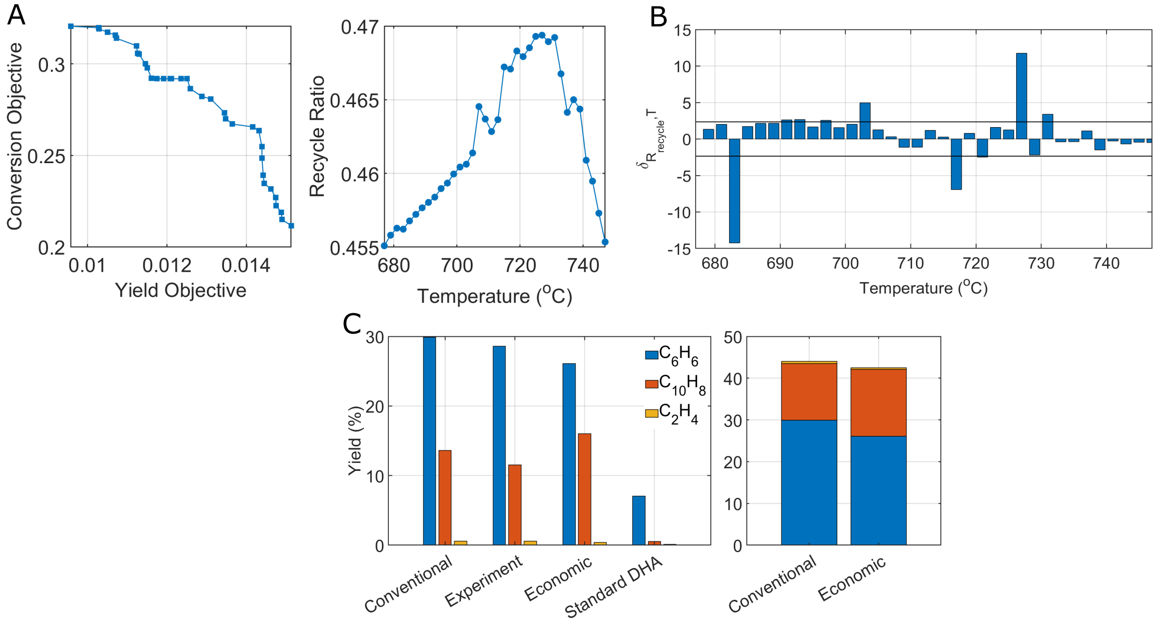

Figure 9: *Optimization analysis of surrogate models. A. Pareto plot of the conversion and yield cost function and optimal recycle ratio at different DHA operating temperatures. B. Optimal recycle ratio sensitivities w.r.t DHA temperature with the threshold computed using 10% of the maximum value of* $\delta_{R_{recycle},T}$. *C. Comparison of optimization outcomes with experimental observation and the stand-alone DHA process.*

Despite knowing the operating temperature obtained from the cost function analysis, determining the optimal recycle ratio and its corresponding operating temperature remains unresolved. This was obtained by solving the optimization problem outlined in Eq. 10 for the operating temperature and flowrates adjusted within the limits obtained from the parametric analysis of DHA, CLC, and TSA (see Figure 9A). The left plot illustrates the economic optimum values of conversion and yields at different DHA temperatures, while the plot on the right showcases the optimal recycle ratio as a function of temperature. The range of the economic optimal recycle ratio is between 0.45 and 0.47. The sensitivity of the optimal recycle ratio for the DHA reaction temperature is computed using $\delta_{\mathrm{R_{recycle}},\mathrm{T}} = \left(\frac{\mathrm{T}}{\mathrm{R_{recycle}}} \cdot \frac{\partial \mathrm{R_{recycle}}}{\partial \mathrm{T}}\right)$ to verify the effect of temperature perturbations on the optimal solutions (Figure 9B). A maximum positive value of the sensitivity is achieved at 725 °C, the recommended operating temperature for DHA. Since most of the optimal recycle ratios are below the 10% threshold, it is safe to conclude that the current optimal recycle ratio and the corresponding temperature are the most effective to operate.

The optimal recycle ratio was cross-verified with the result presented in Figure 8C. The optimum solutions were compared with experiments and the stand-alone DHA process in Figure 9C. The comparison shows that the aromatics yield of operational optimum is greater than the experimental yield. In both cases, the process is operated at R > 0.95. Accounting for economic factors within a rigorous optimization framework, the optimal recycle ratio shifts toward 0.47 resulting in a product yield of greater than 40%. The difference is that naphthalene formation increases at the economic operating point compared to the conventional case illustrated in Figure 9C.

Comparing the operating conditions with the experiments, a recycle ratio above 0.55 is suggested to obtain more than 40% aromatics yield by minimizing the naphthalene formation. When compared to the experiments, aromatics yields have increased by 4% (conventional optimum) and 2% (economic optimum). Despite a 2% reduction in product yield, the economic considerations associated with recycling costs and conversion per pass play a pivotal role in the decision-making. Therefore, the computed optimal recycle ratio ($\mathrm{R}_{recycle} = 0.47$) at 725 °C is identified as the desired economic operating point. The notion of optimal operation has been demonstrated for linear and nonlinear steady-state reactive separation processes[80,82]. The results indicate the presence of a unique optimum for a given set of operating conditions that agree with the findings in Figure 8C of the multi-objective framework.

4 Conclusions

This study presented a spatiotemporal process model for an integrated methane dehydroaromatization (DHA) process proposed in Ref. 16[16]. The mathematical models governing the methane DHA, the reduction of $\mathrm{Fe_3O_4}$ with hydrogen in chemical looping combustion (CLC), and the adsorption of benzene-naphthalene-water on zeolite-13x in temperature swing adsorption (TSA) processes were formulated as convection-diffusion-reaction and convection-reaction partial differential equations. The models for gas-solid CLC and TSA processes leverage the equilibrium theory of nonlinear waves, resulting in rapid reaction and mass transfer between the two phases. These models delineate process operating boundaries and provide a foundation to build steady-state surrogate models. These were subsequently integrated and solved using the simultaneous modular method for varying recycle ratios.

Model predictions for each process and the integrated system were validated against experimental data[15,16,27,77], showing a good agreement[16]. The model recommends the DHA process to run at 725 °C and below 5000 mL/g.h, CLC between 680 and 770 °C, and TSA at 125 mL/g.h. The integrated surrogate model recommended a recycle ratio of $\mathrm{R}_{\mathrm{recycle}} = 0.47$ and a temperature of 725 °C for an optimum economic trade-off between product yield and conversion per pass. Operating the process at the optimum point drives the process to higher aromatics yields than experiments.

The methodology proposed is unique due to the semi-batch nature of the process operation, as almost all the reactive separation processes are operated in continuous mode. This work showcases the potential to systematically optimize the semi-batch modular reactive separation process and can be extended to other semi-batch operated reactive-separation systems with equilibrium-limited endothermic reactions.

Acknowledgements

We acknowledge the support by the RAPID manufacturing institute, USA, supported by the Department of Energy (DOE) Advanced Manufacturing Office (AMO), award number DE-EE0007888-6.5. We acknowledge the Late Prof. Babatunde A. Ogunnaike for his guidance, support, and contributions as an advisor, mentor, and friend.

References

(1) Kittner, N.; Lill, F.; Kammen, D. M. Energy storage deployment and innovation for the clean energy transition. *Nature Energy* **2017**, *2*, 1–6.

(2) Bui, M.; Adjiman, C. S.; Bardow, A.; Anthony, E. J.; Boston, A.; Brown, S.; Fennell, P. S.; Fuss, S.; Galindo, A.; Hackett, L. A.; others Carbon capture and storage (CCS): the way forward. *Energy & Environmental Science* **2018**, *11*, 1062–1176.

(3) Li, X.; Barton, P. I. Optimal design and operation of energy systems under uncertainty. *Journal of Process Control* **2015**, *30*, 1–9.

(4) Nahreen, S.; Praserthdam, S.; Perez Beltran, S.; Balbuena, P. B.; Adhikari, S.; Gupta, R. B. Catalytic upgrading of methane to higher hydrocarbon in a nonoxidative chemical conversion. *Energy & Fuels* **2016**, *30*, 2584–2593.

(5) Luk, H. T.; Mondelli, C.; Ferré, D. C.; Stewart, J. A.; Pérez-Ramírez, J. Status and prospects in higher alcohols synthesis from syngas. *Chemical Society Reviews* **2017**, *46*, 1358–1426.

(6) Tso, W. W.; Demirhan, C. D.; Floudas, C. A.; Pistikopoulos, E. N. Multi-scale energy systems engineering for optimal natural gas utilization. *Catalysis Today* **2020**, *356*, 18–26.

(7) Zichittella, G.; Pérez-Ramírez, J. Status and prospects of the decentralised valorisation of natural gas into energy and energy carriers. *Chemical Society Reviews* **2021**, *50*, 2984–3012.

(8) Hammond, C.; Conrad, S.; Hermans, I. Oxidative methane upgrading. *ChemSusChem* **2012**, *5*, 1668–1686.

(9) Khalilpour, R.; Karimi, I. Evaluation of utilization alternatives for stranded natural gas. *Energy* **2012**, *40*, 317–328.

(10) Baldea, M.; Edgar, T. F.; Stanley, B. L.; Kiss, A. A. Modular manufacturing processes: Status, challenges, and opportunities. *AIChE journal* **2017**, *63*, 4262–4272.

(11) Kosinov, N.; Hensen, E. J. Reactivity, Selectivity, and Stability of Zeolite-Based Catalysts for Methane Dehydroaromatization. *Advanced Materials* **2020**, *32*, 2002565.

(12) Zhang, J.-Z.; Long, M. A.; Howe, R. F. Molybdenum ZSM-5 zeolite catalysts for the conversion of methane to benzene. *Catalysis today* **1998**, *44*, 293–300.

(13) Mevawala, C.; Bai, X.; Kotamreddy, G.; Bhattacharyya, D.; Hu, J. Multiscale Modeling of a Direct Nonoxidative Methane Dehydroaromatization Reactor with a Validated Model for Catalyst Deactivation. *Industrial & Engineering Chemistry Research* **2021**, *60*, 4903–4918.

(14) Zhu, Y.; Al-Ebbinni, N.; Henney, R.; Yi, C.; Barat, R. Extension to multiple temperatures of a three-reaction global kinetic model for methane dehydroaromatization. *Chemical Engineering Science* **2018**, *177*, 132–138.

(15) Brady, C.; Murphy, B.; Xu, B. Enhanced methane dehydroaromatization via coupling with chemical looping. *ACS Catalysis* **2017**, *7*, 3924–3928.

(16) Brady, C.; Debruyne, Q.; Majumder, A.; Goodfellow, B.; Lobo, R.; Calverley, T.; Xu, B. An integrated methane dehydroaromatization and chemical looping process. *Chemical Engineering Journal* **2021**, *406*, 127168.

(17) Moulijn, J. A.; Stankiewicz, A.; Grievink, J.; Górak, A. Process intensification and process systems engineering: a friendly symbiosis. *Computers & Chemical Engineering* **2008**, *32*, 3–11.

(18) Nikačević, N. M.; Huesman, A. E.; Van den Hof, P. M.; Stankiewicz, A. I. Opportunities and challenges for process control in process intensification. *Chemical Engineering and Processing: Process Intensification* **2012**, *52*, 1–15.

(19) Bhavsar, S.; Veser, G. Chemical looping beyond combustion: production of synthesis gas via chemical looping partial oxidation of methane. *Rsc Advances* **2014**, *4*, 47254–47267.

(20) Pahinkar, D. G.; Garimella, S. A novel temperature swing adsorption process for natural gas purification: Part I, model development. *Separation and Purification Technology* **2018**, *203*, 124–142.

(21) Joss, L.; Gazzani, M.; Hefti, M.; Marx, D.; Mazzotti, M. Temperature swing adsorption for the recovery of the heavy component: an equilibrium-based shortcut model. *Industrial & Engineering Chemistry Research* **2015**, *54*, 3027–3038.

(22) Ackley, M. W.; Rege, S. U.; Saxena, H. Application of natural zeolites in the purification and separation of gases. *Microporous and Mesoporous Materials* **2003**, *61*, 25–42.

(23) Gholami, M.; Van Assche, T. R.; Denayer, J. F. Temperature vacuum swing, a combined adsorption cycle for carbon capture. *Current Opinion in Chemical Engineering* **2023**, *39*, 100891.

(24) Razdan, N. K.; Kumar, A.; Bhan, A. Controlling kinetic and diffusive length-scales during absorptive hydrogen removal in methane dehydroaromatization on MoCx/H-ZSM-5 catalysts. *Journal of Catalysis* **2019**, *372*, 370–381.

(25) Han, L.; Zhou, Z.; Bollas, G. M. Heterogeneous modeling of chemical-looping combustion. Part 1: Reactor model. *Chemical Engineering Science* **2013**, *104*, 233–249.

(26) Heidebrecht, P.; Sundmacher, K. Thermodynamic analysis of a cyclic water gas-shift reactor (CWGSR) for hydrogen production. *Chemical Engineering Science* **2009**, *64*, 5057–5065.

(27) Hertel, C.; Heidebrecht, P.; Sundmacher, K. Experimental quantification and modelling of reaction zones in a cyclic watergas shift reactor. *International journal of hydrogen energy* **2012**, *37*, 2195–2203.

(28) Ruthven, D. M.; Wong, F. Generalized statistical model for the prediction of binary adsorption equilibria in zeolites. *Industrial & engineering chemistry fundamentals* **1985**, *24*, 27–32.

(29) Clausse, M.; Bonjour, J.; Meunier, F. Adsorption of gas mixtures in TSA adsorbers under various heat removal conditions. *Chemical Engineering Science* **2004**, *59*, 3657–3670.

(30) Gabruś, E.; Witkiewicz, K.; Nastaj, J. Modeling of regeneration stage of 3A and 4A zeolite molecular sieves in TSA process used for dewatering of aliphatic alcohols. *Chemical Engineering Journal* **2018**, *337*, 416–427.

(31) Zhou, Z.; Han, L.; Bollas, G. M. Model-based analysis of bench-scale fixed-bed units for chemical-looping combustion. *Chemical engineering journal* **2013**, *233*, 331–348.

(32) Erans, M.; Sanz-Pérez, E. S.; Hanak, D. P.; Clulow, Z.; Reiner, D. M.; Mutch, G. A. Direct air capture: process technology, techno-economic and socio-political challenges. *Energy & Environmental Science* **2022**, *15*, 1360–1405.

(33) Al Wahedi, Y.; Torres, A. I.; Al Hashimi, S.; Dowling, N. I.; Daoutidis, P.; Tsapatsis, M. Economic assessment of temperature swing adsorption systems as Claus tail gas clean up units. *Chemical Engineering Science* **2015**, *126*, 186–195.

(34) Pahinkar, D. G.; Garimella, S. A novel temperature swing adsorption process for natural gas purification, part II: performance assessment. *Separation and Purification Technology* **2018**, *204*, 81–89.

(35) Larsson, T.; Govatsmark, M.; Skogestad, S.; Yu, C.-C. Control structure selection for reactor, separator, and recycle processes. *Industrial & engineering chemistry research* **2003**, *42*, 1225–1234.

(36) Morud, J.; Skogestad, S. Effects of recycle on dynamics and control of chemical processing plants. *Computers & chemical engineering* **1994**, *18*, S529–S534.

(37) Griffin, D. W.; Mellichamp, D. A.; Doherty, M. F. Selectivity versus conversion and optimal operating policies for plants with recycle. *AIChE journal* **2008**, *54*, 2597–2609.

(38) Kumar, A.; Daoutidis, P. Nonlinear dynamics and control of process systems with recycle. *Journal of Process Control* **2002**, *12*, 475–484.

(39) Baldea, M.; Daoutidis, P. *Dynamics and nonlinear control of integrated process systems*; Cambridge University Press, 2012.

(40) Baldea, M. From process integration to process intensification. *Computers & Chemical Engineering* **2015**, *81*, 104–114.

(41) Denn, M.; Lavie, R. Dynamics of plants with recycle. *The Chemical Engineering Journal* **1982**, *24*, 55–59.

(42) Pistikopoulos, E. N.; Tian, Y.; Bindlish, R. Operability and control in process intensification and modular design: Challenges and opportunities. *AIChE Journal* **2021**, *67*, e17204.

(43) Tian, Y.; Pistikopoulos, E. N. Synthesis of operable process intensification systems—steady-state design with safety and operability considerations. *Industrial & Engineering Chemistry Research* **2018**, *58*, 6049–6068.

(44) Pattison, R. C.; Baldea, M. Equation-oriented flowsheet simulation and optimization using pseudo-transient models. *AIChE Journal* **2014**, *60*, 4104–4123.

(45) McBride, K.; Sundmacher, K. Overview of surrogate modeling in chemical process engineering. *Chemie Ingenieur Technik* **2019**, *91*, 228–239.

(46) Hao, Z.; Zhang, C.; Lapkin, A. A. Efficient surrogates construction of chemical processes: Case studies on pressure swing adsorption and gas-to-liquids. *AIChE Journal* **2022**, *68*, e17616.

(47) Misener, R.; Biegler, L. Formulating data-driven surrogate models for process optimization. *Computers & Chemical Engineering* **2023**, *179*, 108411.

(48) De Tommaso, J.; Rossi, F.; Moradi, N.; Pirola, C.; Patience, G. S.; Galli, F. Experimental methods in chemical engineering: Process simulation. *The Canadian Journal of Chemical Engineering* **2020**, *98*, 2301–2320.

(49) Pantelides, C.; Barton, P. Equation-oriented dynamic simulation current status and future perspectives. *Computers & chemical engineering* **1993**, *17*, S263–S285.

(50) Biegler, L. T. *Nonlinear programming: concepts, algorithms, and applications to chemical processes*; SIAM, 2010.

(51) Beck, A. *First-order methods in optimization*; SIAM, 2017.

(52) Sun, K.; Ginosar, D. M.; He, T.; Zhang, Y.; Fan, M.; Chen, R. Progress in nonoxidative dehydroaromatization of methane in the last 6 years. *Industrial & Engineering Chemistry Research* **2018**, *57*, 1768–1789.

(53) Li, L.; Borry, R. W.; Iglesia, E. Reaction-transport simulations of non-oxidative methane conversion with continuous hydrogen removal—homogeneous–heterogeneous reaction pathways. *Chemical engineering science* **2001**, *56*, 1869–1881.

(54) Ruthven, D. M.; Doetsch, I. H. Diffusion of hydrocarbons in 13X zeolite. *AIChE journal* **1976**, *22*, 882–886.

(55) Cordero-Lanzac, T.; Aguayo, A. T.; Gayubo, A. G.; Castaño, P.; Bilbao, J. A comprehensive approach for designing different configurations of isothermal reactors with fast catalyst deactivation. *Chemical Engineering Journal* **2020**, *379*, 122260.

(56) Janssens, T. V. A new approach to the modeling of deactivation in the conversion of methanol on zeolite catalysts. *Journal of Catalysis* **2009**, *264*, 130–137.

(57) Bleken, F. L.; Barbera, K.; Bonino, F.; Olsbye, U.; Lillerud, K. P.; Bordiga, S.; Beato, P.; Janssens, T. V.; Svelle, S. Catalyst deactivation by coke formation in microporous and desilicated zeolite H-ZSM-5 during the conversion of methanol to hydrocarbons. *Journal of catalysis* **2013**, *307*, 62–73.

(58) Mazzotti, M.; Rajendran, A. Equilibrium theory–based analysis of nonlinear waves in separation processes. *Annual review of chemical and biomolecular engineering* **2013**, *4*, 119–141.

(59) Swenson, H.; Stadie, N. P. Langmuir's theory of adsorption: A centennial review. *Langmuir* **2019**, *35*, 5409–5426.

(60) Kreiss, H.-O.; Scherer, G. Method of lines for hyperbolic differential equations. *SIAM Journal on Numerical Analysis* **1992**, *29*, 640–646.

(61) Kaisare, N. S. *Computational techniques for process simulation and analysis using Matlab®*; CRC Press, 2017.

(62) Schiesser, W. E.; Griffiths, G. W. *A compendium of partial differential equation models: method of lines analysis with Matlab*; Cambridge University Press, 2009.

(63) Slotine, J.-J. E.; Li, W.; others *Applied nonlinear control*; Prentice hall Englewood Cliffs, NJ, 1991; Vol. 199.

(64) Vidyasagar, M. *Nonlinear systems analysis*; SIAM, 2002.

(65) Davidson, T. A. *A simple and accurate method for calculating viscosity of gaseous mixtures*; US Department of the Interior, Bureau of Mines, 1993; Vol. 9456.

(66) Wilke, C. R. A viscosity equation for gas mixtures. *The journal of chemical physics* **1950**, *18*, 517–519.

(67) Sun, W.; Braatz, R. D. ALVEN: Algebraic learning via elastic net for static and dynamic nonlinear model identification. *Computers & Chemical Engineering* **2020**, *143*, 107103.

(68) Champion, K.; Lusch, B.; Kutz, J. N.; Brunton, S. L. Data-driven discovery of coordinates and governing equations. *Proceedings of the National Academy of Sciences* **2019**, *116*, 22445–22451.

(69) Beck, A.; Eldar, Y. C. Sparsity constrained nonlinear optimization: Optimality conditions and algorithms. *SIAM Journal on Optimization* **2013**, *23*, 1480–1509.

(70) Kochenderfer, M. J.; Wheeler, T. A. *Algorithms for optimization*; Mit Press, 2019.

(71) Hastie, T.; Tibshirani, R.; Friedman, J. H.; Friedman, J. H. *The elements of statistical learning: data mining, inference, and prediction*; Springer, 2009; Vol. 2.

(72) Mendes-Moreira, J.; Soares, C.; Jorge, A. M.; Sousa, J. F. D. Ensemble approaches for regression: A survey. *Acm computing surveys (csur)* **2012**, *45*, 1–40.

(73) Schulz, E.; Speekenbrink, M.; Krause, A. A tutorial on Gaussian process regression: Modelling, exploring, and exploiting functions. *Journal of Mathematical Psychology* **2018**, *85*, 1–16.

(74) Sundaramoorthy, A. S.; Varanasi, S. K.; Huang, B.; Ma, Y.; Zhang, H.; Wang, D. Sparse inverse covariance estimation for causal inference in process data analytics. *IEEE Transactions on Control Systems Technology* **2021**, *30*, 1268–1280.

(75) Tibshirani, R. Regression shrinkage and selection via the lasso. *Journal of the Royal Statistical Society: Series B (Methodological)* **1996**, *58*, 267–288.

(76) Grossmann, I. E. *Advanced optimization for process systems engineering*; Cambridge University Press, 2021.

(77) Li, L.; Borry, R. W.; Iglesia, E. Design and optimization of catalysts and membrane reactors for the non-oxidative conversion of methane. *Chemical engineering science* **2002**, *57*, 4595–4604.

(78) Kullback, S.; Leibler, R. A. On information and sufficiency. *The annals of mathematical statistics* **1951**, *22*, 79–86.

(79) Panaretos, V. M.; Zemel, Y. Statistical aspects of Wasserstein distances. *Annual review of statistics and its application* **2019**, *6*, 405–431.

(80) Kiss, A. A.; Bildea, C. S.; Dimian, A. C. Design and control of recycle systems by non-linear analysis. *Computers & chemical engineering* **2007**, *31*, 601–611.

(81) Frumkin, J.; Fleitmann, L.; Doherty, M. Ultimate Reaction Selectivity Limits for Intensified Reactor-Separators. *Industrial and Engineering Chemistry Research* **2019**, *58*, 6042–6048.

(82) Kumar, V.; Kaistha, N. Real Time Optimization of a Reactor–Separator–Recycle Process I: Steady State Modeling. *Industrial & Engineering Chemistry Research* **2018**, *57*, 12429–12443.

(83) Iliuta, I.; Tahoces, R.; Patience, G. S.; Rifflart, S.; Luck, F. Chemical-looping combustion process: Kinetics and mathematical modeling. *AIChE journal* **2010**, *56*, 1063–1079.

(84) Gómez-Barea, A.; Ollero, P. An approximate method for solving gas–solid non-catalytic reactions. *Chemical Engineering Science* **2006**, *61*, 3725–3735.

(85) Spreitzer, D.; Schenk, J. Reduction of iron oxides with hydrogen—a review. *steel research international* **2019**, *90*, 1900108.

(86) Maier, J. *Physical chemistry of ionic materials: ions and electrons in solids*; John Wiley & Sons, 2023.

(87) Wenzel, M.; Rihko-Struckmann, L.; Sundmacher, K. Continuous production of CO from CO2 by RWGS chemical looping in fixed and fluidized bed reactors. *Chemical Engineering Journal* **2018**, *336*, 278–296.

(88) Hwang, Y.-L. Wave propagation in mass-transfer processes: from chromatography to distillation. *Industrial & engineering chemistry research* **1995**, *34*, 2849–2864.

(89) Rhee, H.-K.; Aris, R.; Amundson, N. R. *First-order partial differential equations*; Courier Corporation, 2014; Vol. 1.

(90) Yang, R. T. *Gas separation by adsorption processes*; World Scientific, 1997; Vol. 1.

(91) Son, K. N.; Richardson, T.-M. J.; Cmarik, G. E. Equilibrium adsorption isotherms for H2O on Zeolite 13X. *Journal of Chemical & Engineering Data* **2019**, *64*, 1063–1071.

(92) Kim, K.-M.; Oh, H.-T.; Lim, S.-J.; Ho, K.; Park, Y.; Lee, C.-H. Adsorption equilibria of water vapor on zeolite 3A, zeolite 13X, and dealuminated Y zeolite. *Journal of Chemical & Engineering Data* **2016**, *61*, 1547–1554.

(93) Rota, R.; Gamba, G.; Paludetto, R.; Carra, S.; Morbidelli, M. Generalized statistical model for multicomponent adsorption equilibria on zeolites. *Industrial & engineering chemistry research* **1988**, *27*, 848–851.

(94) Neidinger, R. D. Introduction to automatic differentiation and MATLAB object-oriented programming. *SIAM review* **2010**, *52*, 545–563.

(95) Parikh, N.; Boyd, S. Proximal algorithms. *Foundations and Trends in optimization* **2014**, *1*, 127–239.

(96) Qu, G.; Li, N. On the exponential stability of primal-dual gradient dynamics. *IEEE Control Systems Letters* **2018**, *3*, 43–48.